Review of Scientific Instruments ARTICLE pubs.aip.org/aip/rsi

Polarized neutron imaging at NeXT (neutron and x-ray tomograph) at Institut Laue Langevin

Cite as: Rev. Sci. Instrum. 95, 063703 (2024); doi: 10.1063/5.0210028
Submitted: 25 March 2024 • Accepted: 3 June 2024 •
Published Online: 17 June 2024

U. K. Oji,[1,2,a)] A. Tengattini,[1] L. Helfen,[1] I. Manke,[2] R. Cubitt,[1] and N. Kardjilov[2]

AFFILIATIONS

[1] Institut Laue-Langevin, Large Scale Structures Group, 71 Avenue des Martyrs CS 20156, 38042, Grenoble Cedex 9, France
[2] Helmholtz Centre Berlin for Materials and Energy, D-14109 Berlin, Germany

[a)] **Author to whom correspondence should be addressed:** u.oji@campus.tu-berlin.de

ABSTRACT

This work describes the implementation of polarized neutron imaging capabilities at the neutron and x-ray tomograph (NeXT) imaging station of the Institut Laue Langevin. This development enhances the capacity of this instrument to study advanced magnetic materials, which are crucial in a variety of engineering applications. Here, the feasibility of polarized neutron imaging at NeXT is demonstrated by visualizing the magnetic field generated by a simple bar magnet. The use of a double-crystal monochromator for wavelength-resolved imaging is also shown to enable both quantitative and qualitative analyses of magnetic materials. This is demonstrated through the determination of magnetization strength in a sample of electric steel (FeSi) in addition to the distribution of its components. Polarimetric imaging is also implemented for the first time to characterize the magnetic field generated by a current-carrying cylindrical wire. These findings collectively underscore the value of incorporating polarized neutron imaging into the already cutting-edge imaging station.

I. INTRODUCTION

Until 2021, the Institut Laue Langevin operated at its beam port, D50 (that is used to accommodate the RAINBOWS reflectometer as well), the neutron and x-ray tomograph (NeXT) tomography station, which allows the simultaneous use of neutrons and x-rays as a probe for material characterization.[1] In recent years, it has served principally for material and energy studies such as the behavior of porous media,[2–4] battery characterization,[5] and biological systems such as plants[6] employing a white cold neutron beam with a peak flux at 2.8 Å for this purpose. At the time of writing, it is the neutron imaging station that offers the highest spatiotemporal resolutions attributable to its high neutron flux up to 3×10^8 n/cm^2/s at the sample location, for a collimation ratio of 330. Given the growing interest for polarized neutron imaging in magnetic characterization, the addition of the option to the NeXT station not only brings it to the state of the art but also will allow quick magnetic characterization of materials with neutrons in addition to potentially higher image resolution as a result of the higher flux.

Since the pioneering work by Kardjilov *et al.*[7] where the technique of polarized neutron imaging was used in the qualitative 3D reconstruction of the trapped magnetic field in superconducting Pb, the technique has mainly facilitated studies of magnetic phenomena in superconducting systems. This includes visualization of the Meissner effect by Dawson *et al.*[8] and the quantitative investigations of field penetration and trapping in type II superconductors.[9] Advancements in the technique's understanding and implementation have allowed defect characterization in these superconducting materials.[10] In addition to the applications in superconductivity studies, polarized neutron imaging techniques have been employed in broader magnetic and electric characterization including the study of electric fields by Jau *et al.*,[11] magnetic characterization of electric motors,[12,13] electric steels,[14] and depolarization measurements for investigating properties of exotic magnetic materials.[15] Furthermore, it is currently under exploration as a method for extending battery characterization.[5]

This paper describes the first attempt at incorporating polarization capabilities into the instrument prior to the very recent upgrade of the tomography station during the 2022 long shutdown,

after which a permanent polarized neutron imaging station was added to the instrument. The components chosen will be discussed, focusing on the reasons behind the choices made. Polarized neutron images of a simple bar magnet will be shown, obtained as proof of concept of the effectiveness of the implementation. Furthermore, facilitated by a double-crystal monochromator, energy-selective polarized neutron images of an electric steel sample (FeSi) are shown here. These are used in the quantitative characterization of magnetic fields in a similar manner as the work done on the Time-Of-Flight imaging station at ISIS[16] by taking advantage of the energy-dependent interaction of the polarized neutron with a magnetic field. Finally, an attempt is made at polarimetric neutron imaging with a current-carrying conductor.

II. POLARIZATION COMPONENTS

A. NeXT imaging station

A detailed description of the NeXT imaging station including its layout and working operations has been given in Ref. 1, although it has recently been upgraded. A paper detailing the new instrument is under redaction, although, for the specific purpose of this work, the description in the original work provides a solid baseline. The instrument could not initially perform polarized neutron imaging and was generally focused on white beam imaging. The dependence of the polarization precession angle on neutron wavelength necessitated the temporary installation of a monochromator in addition to the polarizing, flipping, and collimation devices. These are now permanently integrated into the instrument. A schematic illustration of the setup for polarized neutron imaging after monochromatization of the beam is given in Fig. 1.

1. Monochromator

A double-crystal monochromator (DCM) was installed in the former reflectometer hutch of the D50 instrument to facilitate energy selection of the incident neutron beam. The system consists of two diffracting highly oriented pyrolytic graphite (HOPG) crystals employing their (002) reflections and maintaining both fixed beam exit direction and position. The mosaicity was 0.8° allowing the selection of wavelength bands between 2.0 and 6.5 Å without changing the position of the beam.[17] Calibration of the device was performed via energy-selective radiography of a sample of iron powder. A scan is performed from 3.0 to 4.5 Å using a step size of 0.02 Å with each radiograph obtained having an exposure time of 30 s. All radiographs were corrected with open beam images for beam inhomogeneities and dark images for electronic noise from the detector. Figure 2 (left) shows the radiograph of the Fe powder, and Fig. 2 (right) shows the graph of the normalized transmission vs wavelength of the neutron beam. We can see that the Bragg edge is located at a wavelength of about 4.1 Å, which is expected.[18] This gives confidence for the proper alignment of the monochromator to facilitate further experimentation.

2. Polarization devices

Polarization and analysis devices play a crucial role in a polarized neutron experiment, ultimately determining the quality of the obtained neutron images. Therefore, selecting these devices is of utmost importance to maximize the image quality. In the context of optimizing achievable resolution, two key factors are essential: providing a broad field of view for the neutron beam and compactness (notably to minimize the distance of the sample to the detector, crucial for the resolution of the images). To extend the versatility of the setup, these devices should be capable of accommodating a wide range of neutron wavelengths for magnetic characterization. This flexibility is especially important in cases involving small fields, where a weak wavelength dependence necessitates the use of polarizing devices tailored to the neutron spectrum of the beamline or instrument.

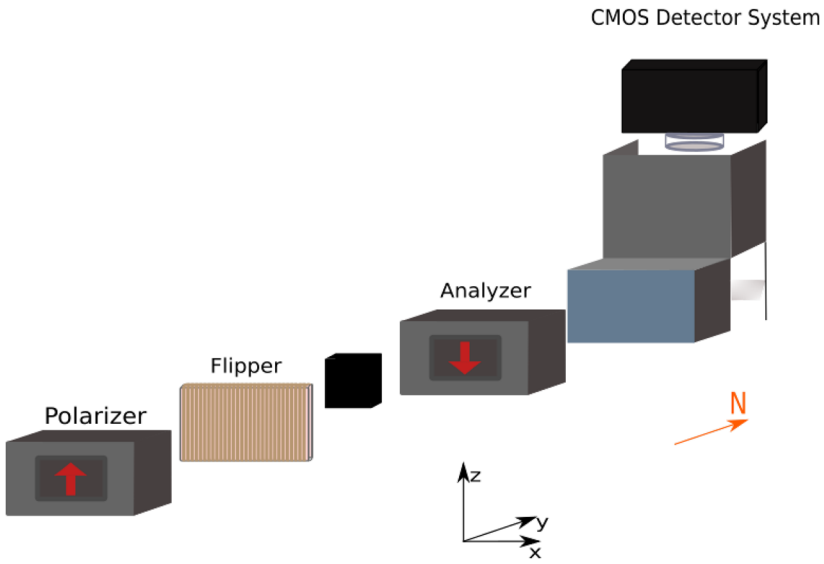

FIG. 1. Schematic of the experimental setup with the double-crystal monochromator positioned before the polarizer.

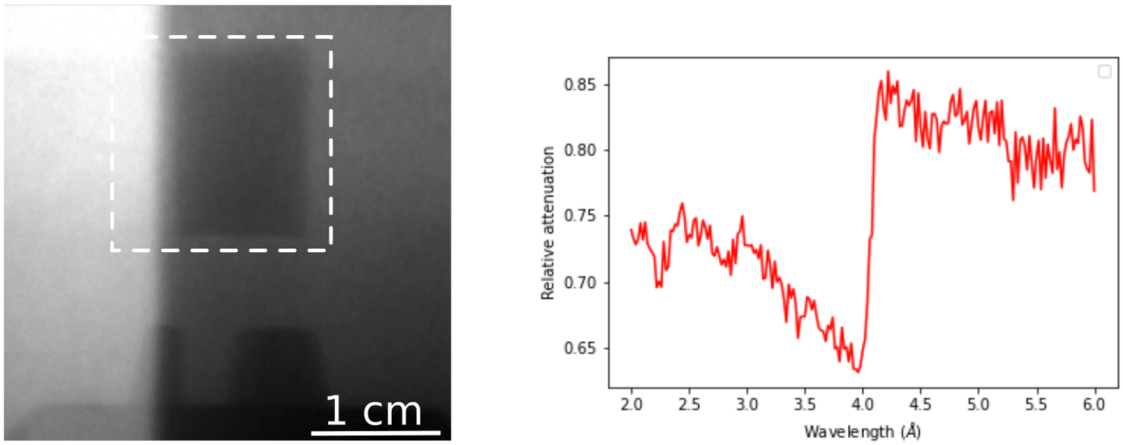

FIG. 2. Transmission radiograph of the sample of iron powder (left, dashed box) with the corresponding normalized transmission intensity as a function of incident neutron wavelength (right) where we can see the Bragg edge of the iron powder at about 4.1 Å.

Considering the above criteria, the choice was made to employ solid-state benders made by Swiss Neutronics for both polarization and analysis devices. A polarizing transmission bender was positioned before the sample position as the polarizer unit. The device's field of view has a width and height of 30 × 50 mm^2. Its substrate is made from a single-crystal Si wafer of thickness 0.15 mm and has a supermirror coating of Fe/Si with an m-value (critical angle relative to nickel) of 3.3. The magnetic polarizing mirrors are aligned vertically and are magnetized by the integrated housing in the device made from Nd-based magnets.[19,20] They are transmission-based, meaning that only one spin channel is allowed through, which we define as spin up, while the other channel (spin down) is reflected. In this setup, the neutrons in the beam with different spin orientations encounter different refractive properties in the magnetic material depending on their alignment with, or against, the applied vertical magnetic field. The curved Si plates are designed to ensure that when the beam's polarization aligns with the magnetic field, it undergoes total reflection, while the other component passes through with minimal alterations. Importantly, there is no absorbing layer on the Si wafer plates, allowing the two spin components to be spatially separated. A Soller collimator is used in combination with the polarizer to allow or remove the transmitted or reflected neutron spin component, or vice versa, through angular adjustment. It is made of stacked Si (0.3 mm) wafers coated with TiGd (0.25 μm thickness). For the experiment, the collimator was set to retain the transmitted spin channel, and it provided an angular divergence of 0.34° in the horizontal and 1.28° in the vertical direction.

The analysis device was installed after the sample position. Its operating principle is similar to that of the polarizing devices, with the key difference being that it works in reflection. This is a consequence of the gadolinium coatings on the backside of its silicon lamellae, which absorb the non-reflected neutrons. The critical neutron wavelength for these polarizing devices is 2.1 Å, a value well below the peak neutron flux wavelength of 2.8 Å on NeXT, which allows for efficient polarized neutron imaging at the imaging station.[1]

3. Spin controlling devices

Control of the neutron polarization direction is affected by a Mezei flipper. The device uses a static magnetic field orthogonal to the neutron beam polarization direction for non-adiabatic rotation of the spin orientation. Adjusting the current flowing through the flipper coils allows for adjusting the field strength for the rotation of the polarization axis.

B. Setup

The devices are assembled for the experiment in the order of collimator, analyzer, polarizer, and spin flipper, as illustrated in Fig. 1. This order of installation optimizes for beam transmission and polarization. The installation of each device, with the exception of the spin flipper, is facilitated by the use of rotation stages. The collimator and then analyzer are first installed and aligned with a precision of 0.1° to maximize the transmission of the incident neutron beam. The polarizer, on the other hand, is then aligned to maximize the beam polarization to the same precision. This is facilitated via a modification of the Shim test. A demagnetized Fe ring is positioned in the field of view of the beam to cover it partially. The ring is expected to completely depolarize an incident polarized beam. The polarizing device is rotated in steps of 0.1° to find the position where there is the largest contrast between regions of the ring and the empty beam. Finally, the spin flipper was installed and current-calibrated for efficient polarization rotation, i.e., determining the applied currents that correspond to maximum and minimum transmission.

The detector comprised a 100-micron thick LiF/ZnS scintillator, imaged by a CMOS camera (Hamamatsu Orca Flash). A 50 mm f/1.2 lens was mounted on the camera to facilitate imaging. The field of view is limited by the dimensions of the polarizing devices. The sample is located 15 cm away from the detector. The collimation ratio L/D of 333 results in a neutron penumbra of about 0.5 mm. All radiographs were taken with an exposure time of 30 s. They were corrected for beam inhomogeneities and electronic noise in a manner similar

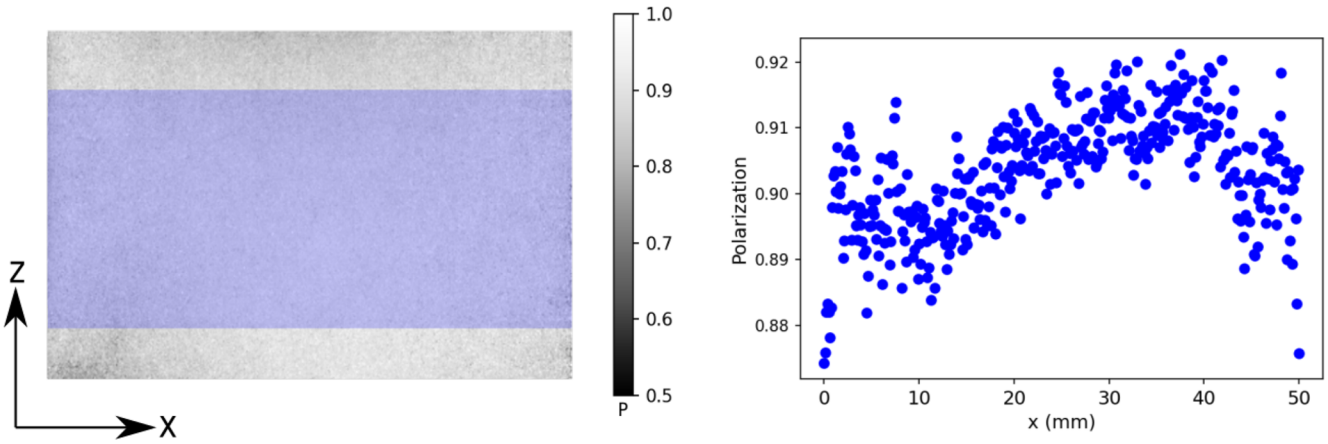

FIG. 3. Open beam polarization after the setup (left) with the homogeneity profile corresponding to the region highlighted in blue. The standard deviation in this region is 0.9% from the mean polarization.

to the case of those used in the monochromator setup and calibration.

The polarization of the beam was determined to be 88% at a neutron wavelength of 3.0 Å. Figure 3 shows an image of the open beam polarization and charts the mean polarization as a function of the lateral position (blue highlight). The beam shows good homogeneity, and the average polarization over the highlighted region is found to be 90.3%, with a standard deviation of 0.9%. Polarized neutron images obtained were normalized with open beam polarized neutron images to correct both for polarizing efficiencies and attenuation signals from the sample absorption.[21]

A simple bar magnet producing a magnetic field of about 1 T at the surface, as measured with a Hall probe, was used as a proof-of-concept sample to test the setup. The polarizer and analyzer are set to have their spin channels parallel to each other by applying the appropriate current to the Mezei flipper. The resultant transmission image is shown in Fig. 4. The grayscale contrast in the image is representative of the total precession angle of the neutron spin passing through the magnetic field from the magnet. The maximum or minimum intensity corresponds to the neutron beam polarization having a parallel or antiparallel orientation relative to the analyzer, respectively. Given the high magnitude of the magnetic field produced, image degeneracies are expected due to the neutron beam polarization having a total rotation of more than π close to the magnet.

The double crystal monochromator was then employed to perform energy-selective polarized neutron imaging. The polarization of the beam as a function of the incident neutron wavelength is shown in Fig. 5. There is an observable decrease in the polarization of the neutron beam with an increase in wavelength attributable to reductions in the efficiency of the polarizing devices at larger wavelengths. This, coupled with the wavelength spread from the mosaicity, means that there is a chance of reducing the polarization at higher wavelengths. The dip at 3.8 Å comes from a fixed monochromator upstream. These do not present a significant limitation for their use in energy-selective polarized neutron imaging as will be shown in Sec. III.

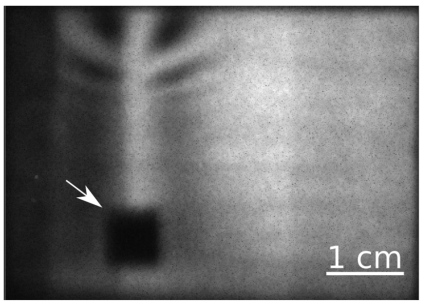

FIG. 4. Transmission image of a generic bar magnet with a surface magnetization of about 1 T. The observed grayscale contrast results from the precession of the neutron beam polarization through the magnetic field from the magnet. The white arrow indicates the position of the magnet.

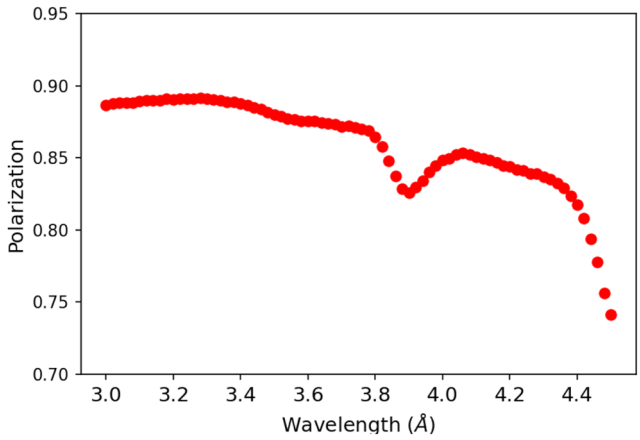

FIG. 5. Polarization of the incident neutron beam as a function of wavelength.

III. ENERGY-SELECTIVE POLARIZED NEUTRON IMAGING

In this section, a case study is presented for energy-selective polarized neutron imaging on NeXT. A sample of electric steel is first investigated to quantify the magnitude of its internal magnetization. The relationship between the beam polarization and the wavelength when interacting with a magnetic field is the key to the study.

A. Magnetic characterization of electric steel (FeSi)

FeSi alloys are typically used as the core material in industrial electric transformers.[22] Their high permeability combined with the minimal hysteresis facilitates a reduction in losses (energy dissipation). Further reduction of losses can be achieved by grain orientation and insulation to reduce Eddy currents.[23,24] The grain orientation serves to improve the magnetic properties of the material, whereas the insulation is known to induce uniaxial stress along the rolling direction, which reinforces the effects of the grain orientation.[25–28] Obtaining and understanding information about the underlying domain structure in a non-destructive manner is, thus, imperative for the continued development of the material. Non-destructive characterization is required since the removal of the insulating layer for characterization[22,29,30] compromises their magnetic properties. The utility of neutron imaging as a probe for the study of FeSi sheet characterization has already been shown through neutron grating interferometry[26,31,32] and polarized neutron imaging.[14] This section presents a first attempt at non-destructive quantification of the magnetization strength and further determination of the magnetization component distribution in a sample of FeSi at the NeXT imaging station. To this end, transformer steel (FeSi) with 3% Si and a thickness of 230 microns was employed. An assumption was made, based on the sample's aspect ratio, that the internal magnetization is oriented along the plane of the sample surface, i.e., the x-z plane in Fig. 1. A further assumption was made that the magnetization was homogeneous through the sample thickness. These two assumptions allowed a pixel-wise estimation of the sample magnetization, including its planar components using the energy-selective polarized neutron imaging.

Figure 6 shows the changes in polarization images as a function of the neutron wavelength. There is a visible change in the final polarization images with the increase in the neutron wavelength. This is a result of the wavelength dependence of the total precession angle, θ, of the neutron polarization in a magnetic field B, which can be described as[33]

$$P = \cos(\theta), \tag{1}$$

$$P = \cos\left(\gamma \frac{\lambda m}{h} \int B dx\right), \tag{2}$$

where P is the beam polarization, λ is the neutron wavelength, m is the neutron mass, and h is Planck's constant.

This implies a sinusoidal correlation between the magnetization and the final polarization. The magnitude of the magnetization in the regions can, hence, be obtained by fitting a simple 1D wave displacement function [Eq. (3)] to determine the frequency (ω) of the signal. This frequency is entirely dependent on the magnitude of the magnetic field or magnetization that the neutrons interact with,

$$y = A \cos(\omega\lambda) + c. \tag{3}$$

Figure 7 shows the relation between the final polarization and the wavelength in the highlighted regions of the image. With negligible damping in the signal, Eq. (3) is sufficient for its fitting and subsequent determination of the values of magnetic field strength. In the yellow, blue, and orange boxed regions, this was found to be 1.89, 1.89, and 1.9 T, respectively. These are typical values found for samples of FeSi.[34,35]

Repeating this same analysis in a pixel-wise manner, it is possible to determine the spatial distribution of the magnetization in the material. These images are 2×2 binned to improve the statistics. This is also done for the sample after a rotation through the y axis by 90° and the resultant B distributions for both orientations are shown in Fig. 8. At the 0° orientation, the beam polarization interacts with the projection of the magnetization in the x direction, while in the 90° orientation, the polarization interacts with the magnetization projection in the z direction so that the images represent the spatial distribution of the x and z Cartesian components of the magnetization in the FeSi sample based on the assumptions detailed above. The difference in the distribution of the B component occurs

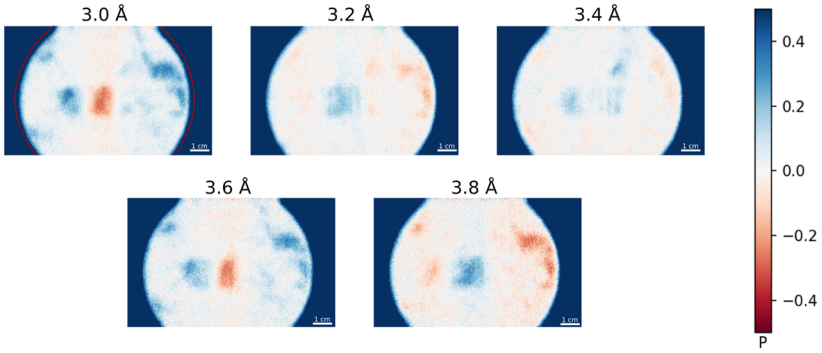

FIG. 6. Polarized neutron images of the FeSi sample at different wavelengths highlighting the changes in contrast and, therefore, the effect on total polarization from the wavelength of the incident neutron beam. The sample position is indicated by the red dashed line.

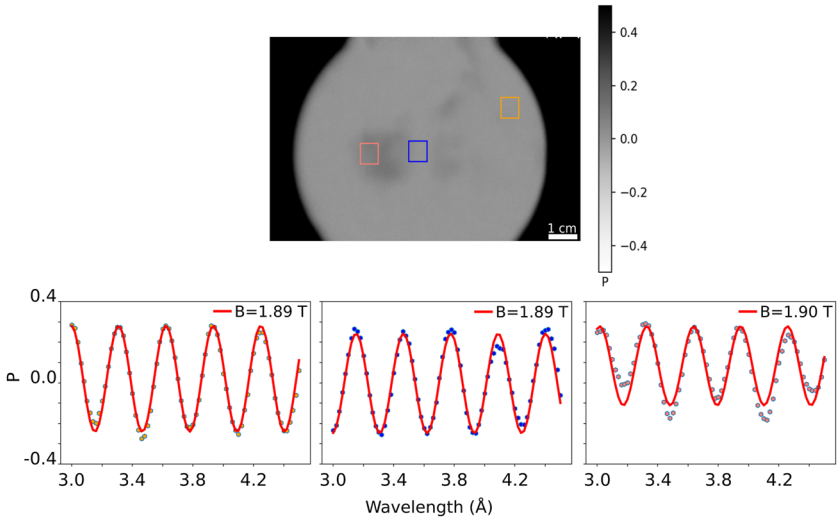

FIG. 7. Mean polarized neutron image of FeSi sample through the wavelength range (top) with the polarization signal as a function of incident neutron wavelength corresponding to the boxed regions (bottom).

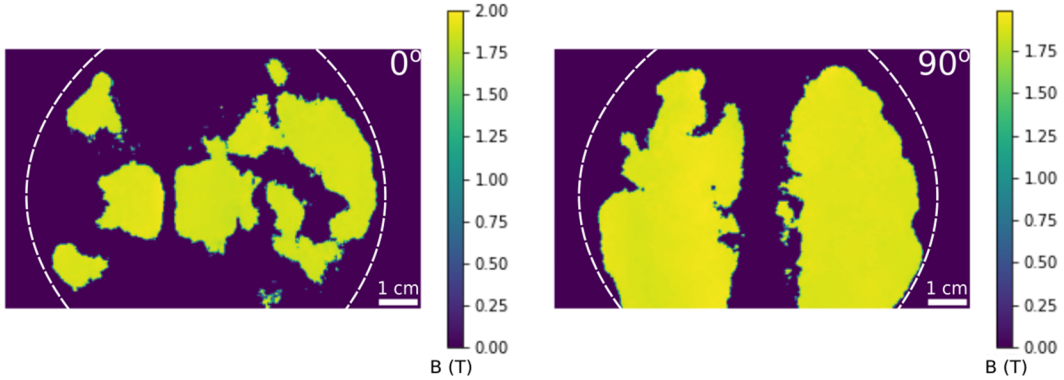

FIG. 8. 2D map of the determined magnetic field strength of the FeSi sample with the sample at 0° orientation (left) and 90° orientation (right). The sample position is indicated by the white dashed line.

because when the polarization orientation precisely aligns with that of the magnetic moment, it leads to the absence of a signal, and thus, no calculated field magnitude. Consequently, in regions where a field is calculated for one polarization direction but not the other, it indicates that the magnetic moment is perfectly perpendicular or parallel, respectively.

Physical interpretations for the exact values of the amplitude and offset terms obtained from the fit are still under debate and will not be discussed further in this work.

IV. POLARIMETRIC NEUTRON RADIOGRAPHY OF A CURRENT-CARRYING WIRE

A further study was performed testing the imaging station's capability for polarimetric neutron imaging. The setup is slightly modified to facilitate this via the addition of three additional π Mezei flippers: an additional flipper before the sample position and two after the sample position. The purpose of the two positioned before the sample position is to orient the incident beam polarization in one of the three Cartesian directions, while the two positioned after the sample facilitate analysis of the final polarization projection in one of the three Cartesian directions after interaction with the sample. In this configuration, the sample distance from the analyzer is 50 cm and the polarization of the neutron beam is 75% at 3.0 Å.

A niobium wire of diameter 1 mm with a current of 2.5 A was used for this study and was oriented orthogonal to the neutron beam as illustrated in Fig. 9(a). Radiograms are acquired with a 30-s exposure time for each of the nine sets of combinations representing incident beam orientation and analysis orientation (e.g., XX denotes incident polarization along the X direction, with final polarization component analysis also along the X direction). The radiograms are corrected for beam inhomogeneity and dark currents in the usual manner in addition to a division by a radiogram of the wire without any current passing through it (to normalize the contributions of the material density to the radiographs).

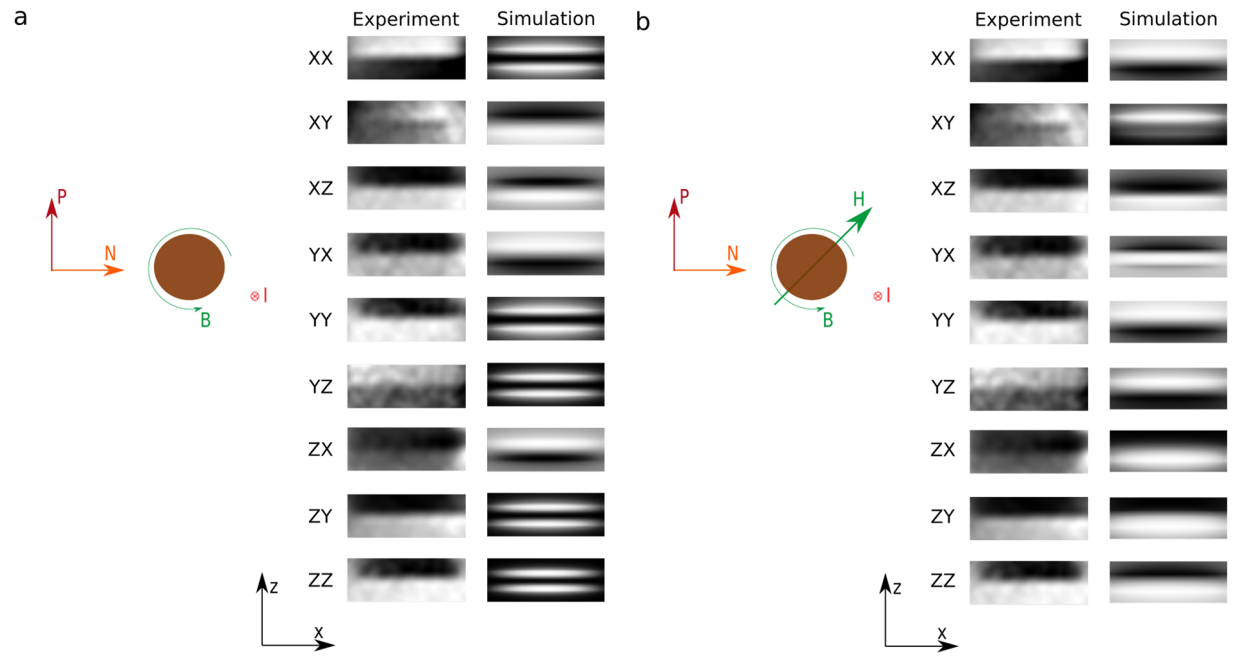

FIG. 9. (a) Comparison between the theoretical and the experimentally obtained polarized neutron image for each combination of incident polarized neutron beam (oriented in one of the X, Y, and Z Cartesian directions) and analyzed for a Cartesian component. (b) A comparison of the experimental and simulated results considering the effects of external fields such as the guide field, including a schematic of the relative orientations of the current carrying wire and the incident neutron beam polarization highlighting the direction of this external field.

Figure 9(a) presents a comparison between the experimental results and those from a simulation. It shows no agreement between the two result sets. Specifically, the presence of asymmetries in the experimental results from the XX, YY, and ZZ configurations do not appear in a theoretical case. This is a result of the adiabatic condition on the final beam polarization. Specifically, in the experiment, both the guide field and the field from the current source connected to the wire contribute to the modification of the split between regions of adiabatic and non-adiabatic rotation of the polarization, which results in the observed asymmetries.

The Hall measurements during the experiment indicate that the guide field at the sample position is about 20 G. Figure 9(b) shows a comparison of the experimental and simulated results after accounting for the presence of a homogeneous field at the sample position in the simulation. The value of the field that yields the most similarity in the simulated result is about 25 G in the direction illustrated in the accompanying schematic [Fig. 9(b)]. While the simulation and the experimental results are in good agreement for most configurations, there is still a mismatch for the YY configuration. This could be a result of the use of a homogeneous external field in the simulation space, which could not strictly correspond to the experimental conditions.

V. CONCLUSION

This paper showcases the implementation of polarized neutron imaging at the NeXT imaging station located at Institut Laue Langevin. It highlights the importance of installing a double crystal monochromator for the quantitative characterization of magnetic materials due to the dependence of the precession on the incident neutron wavelength. Imaging of a simple bar magnet was used as an initial proof of concept for validating the setup. Afterward, taking advantage of the energy-selective capability facilitated by the double crystal monochromator, a sample of FeSi was characterized to determine the strength of the magnetic field across the sample and the distribution of its Cartesian components. Finally, a polarimetric setup was tested with a current carrying wire and the results highlight the need to properly account for the effects of external fields.

ACKNOWLEDGMENTS

We are grateful for the support by K. Buckley. We would like to thank the Institut Laue Langevin for the provision of internal beamtime for the neutron experiment. Instrumentation development for this project was jointly funded by the Institut Laue Langevin and the Helmholtz Zentrum Berlin.

AUTHOR DECLARATIONS

Conflict of Interest

The authors have no conflicts to disclose.

Author Contributions

U. K. Oji: Conceptualization (equal); Data curation (lead); Formal analysis (lead); Investigation (lead); Methodology (equal); Visualization (lead); Writing – original draft (lead); Writing – review &

editing (equal). **A. Tengattini**: Conceptualization (equal); Formal analysis (equal); Investigation (equal); Resources (equal); Writing – review & editing (equal). **L. Helfen**: Conceptualization (equal); Investigation (equal); Resources (equal); Writing – review & editing (equal). **I. Manke**: Resources (equal); Supervision (equal). **R. Cubitt**: Supervision (equal); Writing – review & editing (equal). **N. Kardjilov**: Conceptualization (equal); Investigation (equal); Methodology (equal); Supervision (equal); Validation (equal); Writing – review & editing (equal).

DATA AVAILABILITY

The data that support the findings of this study are available from the corresponding author upon reasonable request.

REFERENCES

[1] A. Tengattini, N. Lenoir, E. Andò, B. Giroud, D. Atkins, J. Beaucour, and G. Viggiani, "NeXT-Grenoble, the neutron and x-ray tomograph in Grenoble," Nucl. Instrum. Methods Phys. Res., Sect. A **968**, 163939 (2020).

[2] M. Etxegarai, E. Tudisco, A. Tengattini, S. Hall, and G. Viggiani, "Hydromechanical behavior of porous rock studied with neutron tomography," in 3rd International Conference on Tomography of Materials and Structures, 2017.

[3] H. Lewis, G. Couples, A. Tengattini, J. Buckman, E. Tudisco, M. Etxegarai, G. Viggiani, and S. A. Hall, "Interactions between imbibition and pressure-driven flow in a microporous deformed limestone," Transp. Porous Media **146**, 559–585 (2023).

[4] Y. Li, S. D. Pont, A. Tengattini, and S.-S. Huang, "Investigation of the thermo-hydral behaviour of concrete with recycled fibres via neutron and x-ray tomographies," in 7th International Workshop on Concrete Spalling Due to Fire Exposure, Berlin, 2022.

[5] R. F. Ziesche, N. Kardjilov, W. Kockelmann, D. J. Brett, and P. R. Shearing, "Neutron imaging of lithium batteries," Joule **6**, 35–52 (2022).

[6] C. Tötzke, N. Kardjilov, N. Lenoir, I. Manke, S. E. Oswald, and A. Tengattini, "What comes NeXT?—High-speed neutron tomography at ILL," Opt. Express **27**, 28640 (2019).

[7] N. Kardjilov, I. Manke, M. Strobl, A. Hilger, W. Treimer, M. Meissner, T. Krist, and J. Banhart, "Three-dimensional imaging of magnetic fields with polarized neutrons," Nat. Phys. **4**, 399–403 (2008).

[8] M. Dawson, I. Manke, N. Kardjilov, A. Hilger, M. Strobl, and J. Banhart, "Imaging with polarized neutrons," New J. Phys. **11**, 043013 (2009).

[9] A. Hilger, I. Manke, N. Kardjilov, M. Osenberg, H. Markötter, and J. Banhart, "Tensorial neutron tomography of three-dimensional magnetic vector fields in bulk materials," Nat. Commun. **9**, 4023 (2018).

[10] A.-E. Ţuţueanu, M. Sales, K. Eliasen, M.-E. Lăcătuşu, J.-C. Grivel, N. Kardjilov, I. Manke, M. Krzyzagorski, Y. Sassa, M. Andersson, S. Schmidt, and K. Lefmann, "Non-destructive characterisation of dopant spatial distribution in cuprate superconductors," Physica C **575**, 1353691 (2020).

[11] Y.-Y. Jau, D. S. Hussey, T. R. Gentile, and W. Chen, "Electric field imaging using polarized neutrons," Phys. Rev. Lett. **125**, 110801 (2020).

[12] S. Sasada, K. Hiroi, K. Osanai, T. Shinohara, K. Watanabe, and A. Uritani, "High-spatial-resolution measurement of magnetization distribution using polarized neutron imaging," Jpn. J. Appl. Phys. **60**, 126003 (2021).

[13] K. Hiroi, T. Shinohara, H. Hayashida, J. D. Parker, K. Oikawa, M. Harada, Y. Su, and T. Kai, "Magnetic field imaging of a model electric motor using polarized pulsed neutrons at J-PARC/MLF," J. Phys.: Conf. Ser. **862**, 012008 (2017).

[14] I. Dhiman, R. Ziesche, L. Riik, I. Manke, A. Hilger, B. Radhakrishnan, T. Burress, W. Treimer, and N. Kardjilov, "Visualization of magnetic domain structure in FeSi based high permeability steel plates by neutron imaging," Mater. Lett. **259**, 126816 (2020).

[15] P. Jorba, M. Schulz, D. S. Hussey, M. Abir, M. Seifert, V. Tsurkan, A. Loidl, C. Pfleiderer, and B. Khaykovich, "High-resolution neutron depolarization microscopy of the ferromagnetic transitions in Ni_3Al and $HgCr_2Se_4$ under pressure," J. Magn. Magn. Mater. **475**, 176–183 (2019).

[16] U. Oji, V. Pacheco, M. Sahlberg, A. Backs, R. Woracek, D. Pooley, G. Nilsen, K. Nemkovski, W. Kockelmann, A. Tremsin, A. Hilger, R. Ziesche, I. Manke, R. Cubitt, and N. Kardjilov, "Implementation of time of flight polarized neutron imaging at IMAT-ISIS," Mater. Des. **235**, 112429 (2023).

[17] W. Treimer, M. Strobl, N. Kardjilov, A. Hilger, and I. Manke, "Wavelength tunable device for neutron radiography and tomography," Appl. Phys. Lett. **89**, 203504 (2006).

[18] M. R. Daymond, P. J. Withers, and E. Lehmann, "Materials science and engineering instruments," in *Performance of a Suite of Generic Instruments on ESS:ESS Instrumentation Group Reports, SAC Workshop*, 3–5 May 2001 (ESS Instrumentation Group, 2001), pp. 57–64.

[19] T. Krist, "Solid state and conventional neutron optical elements," Nucl. Instrum. Methods Phys. Res., Sect. A **529**, 50–53 (2004).

[20] T. Krist and F. Mezei, "Solid state neutron polarizers and collimators," in *International Symposium on Optical Science and Technology*, edited by J. L. Wood and I. S. Anderson (SPIE, San Diego, CA, 2001), pp. 88–95.

[21] S. Mitsuda and Y. Endoh, "Neutron depolarization studies on magnetization process using pulsed polarized neutrons," J. Phys. Soc. Jpn. **54**, 1570–1580 (1985).

[22] A. Hubert and R. Schäfer, *Magnetic Domains: The Analysis of Magnetic Microstructures* (Springer, Berlin, NY, 1998).

[23] I. Gutierrez-Urrutia, A. Böttcher, L. Lahn, and D. Raabe, "Microstructure–magnetic property relations in grain-oriented electrical steels: Quantitative analysis of the sharpness of the Goss orientation," J. Mater. Sci. **49**, 269–276 (2014).

[24] S. Shin, R. Schäfer, and B. C. De Cooman, "Three-dimensional visualization of the magnetic microstructure in bulk Fe-6.6 Pct Si," Metall. Mater. Trans. A **44**, 4239–4247 (2013).

[25] J. Trützschler, K. Sentosun, B. Mozooni, R. Mattheis, and J. McCord, "Magnetic domain wall gratings for magnetization reversal tuning and confined dynamic mode localization," Sci. Rep. **6**, 30761 (2016).

[26] B. Betz, P. Rauscher, R. P. Harti, R. Schäfer, H. Van Swygenhoven, A. Kaestner, J. Hovind, E. Lehmann, and C. Grünzweig, "*In-situ* visualization of stress-dependent bulk magnetic domain formation by neutron grating interferometry," Appl. Phys. Lett. **108**, 012405 (2016).

[27] H. Richert, H. Schmidt, S. Lindner, M. Lindner, B. Wenzel, R. Holzhey, and R. Schäfer, "Dynamic magneto-optical imaging of domains in grain-oriented electrical steel," Steel Res. Int. **87**, 232–240 (2016).

[28] P. Rauscher, B. Betz, J. Hauptmann, A. Wetzig, E. Beyer, and C. Grünzweig, "The influence of laser scribing on magnetic domain formation in grain oriented electrical steel visualized by directional neutron dark-field imaging," Sci. Rep. **6**, 38307 (2016).

[29] E. Beyer, L. Lahn, C. Schepers, and T. Stucky, "The influence of compressive stress applied by hard coatings on the power loss of grain oriented electrical steel sheet," J. Magn. Magn. Mater. **323**, 1985–1991 (2011).

[30] A. Moses, "Effects of applied stress on the magnetic properties of high permeability silicon-iron," IEEE Trans. Magn. **15**, 1575–1579 (1979).

[31] B. Betz, P. Rauscher, R. P. Harti, R. Schäfer, A. Irastorza-Landa, H. Van Swygenhoven, A. Kaestner, J. Hovind, E. Pomjakushina, E. Lehmann, and C. Grünzweig, "Magnetization response of the bulk and supplementary magnetic domain structure in high-permeability steel laminations visualized *in situ* by neutron dark-field imaging," Phys. Rev. Appl. **6**, 024023 (2016).

[32] B. Betz, P. Rauscher, R. P. Harti, R. Schäfer, H. Van Swygenhoven, A. Kaestner, J. Hovind, E. Lehmann, and C. Grünzweig, "Frequency-induced bulk magnetic domain-wall freezing visualized by neutron dark-field imaging," Phys. Rev. Appl. **6**, 024024 (2016).

[33] T. Shinohara, K. Sakai, M. Ohi, T. Kai, M. Harada, K. Oikawa, F. Maekawa, J. Suzuki, T. Oku, S. Takata, K. Aizawa, M. Arai, and Y. Kiyanagi, "Quantitative magnetic field imaging by polarized pulsed neutrons at J-PARC," Nucl. Instrum. Methods Phys. Res., Sect. A **651**, 121–125 (2011).

[34] G. Ouyang, X. Chen, Y. Liang, C. Macziewski, and J. Cui, "Review of Fe-6.5 wt. %Si high silicon steel—A promising soft magnetic material for sub-kHz application," J. Magn. Magn. Mater. **481**, 234–250 (2019).

[35] M. A. Laughton and D. F. Warne, *Electrical Engineer's Reference Book*, 16th ed. (Newnes, Oxford, England, Burlington, MA, 2003).